Kinetic modeling reveals additional regulation at co-transcriptional level by post-transcriptional sRNA regulators

Matthew A. Reyer^{1,2}, Shriram Chennakesavalu^{3,†}, Emily M. Heideman^{3,†}, Xiangqian Ma⁴, Magda Bujnowska³, Lu Hong^{1,2}, Aaron R. Dinner^{1,2,5}, Carin K. Vanderpool⁴, Jingyi Fei^{1,2,3,*}

Summary

Small RNAs (sRNAs) are important gene regulators in bacteria. Many sRNAs act post-transcriptionally by affecting translation and degradation of the target mRNAs upon base-pairing interactions. Here we present a general approach combining imaging and mathematical modeling to determine kinetic parameters at different levels of sRNA-mediated gene regulation that contribute to overall regulation efficacy. Our data reveal that certain sRNAs previously characterized as post-transcriptional regulators can regulate some targets co-transcriptionally, leading to a revised model that sRNA-mediated regulation can occur early in an mRNA's lifetime, as soon as the sRNA binding site is transcribed. This co-transcriptional regulation is likely mediated by Rho-dependent termination when transcription-coupled translation is reduced upon sRNA binding. Our data also reveal several important kinetic steps that contribute to the differential regulation of mRNA targets by an sRNA. Particularly, binding of sRNA to the target mRNA may dictate the regulation hierarchy observed within an sRNA regulon.

Keywords

bacterial small RNA; gene regulation; fluorescence microscopy; mathematical modelling

Present addresses:

Shriram Chennakesavalu, Department of Chemistry, Stanford University, Stanford, CA 94305 Lu Hong, Department of Bioengineering & Therapeutic Sciences at UCSF, San Francisco, CA 94143-2530

Emily M. Heideman, Morsani College of Medicine, University of South Florida, Tampa, FL 33612 Magda Bujnowska, Medical Scientist Training Program, School of Medicine, University of Virginia, Charlottesville, VA 22903

¹ Graduate Program in Biophysical Sciences, The University of Chicago, Chicago, IL, 60637

² Institute for Biophysical Dynamics, The University of Chicago, Chicago, IL, 60637

³ Department of Biochemistry and Molecular Biology, The University of Chicago, Chicago, IL, 60637

⁴ Department of Microbiology, University of Illinois at Urbana-Champaign, Urbana, IL, 61820

⁵ Department of Chemistry, The University of Chicago, Chicago, IL, 60637

[†] These authors contributed equally to this work

^{*}Lead Contact: jingyifei@uchicago.edu (JF)

Introduction

To cope with changes in both natural and host environments, microbes have evolved diverse mechanisms to sense and respond to stress conditions. Small RNAs (sRNAs) are common mediators of gene regulation in bacteria, and have been observed to provide survival benefits during infections, biofilm formation, and exposure to toxins and antibiotics (Caldelari et al., 2013; Felden and Cattoir, 2018; Gerdes and Wagner, 2007; Holmqvist and Wagner, 2017; Mika and Hengge, 2013). In the canonical scheme of sRNA-mediated gene regulation (Figure 1A), sRNAs, often along with a chaperone protein, Hfq, target mRNAs via incomplete Watson-Crick basepairing (Gottesman and Storz, 2011). As many sRNA binding sites on target mRNAs partially overlap with the ribosome binding site (RBS), binding of sRNAs can affect mRNA translation. In addition, the stability of the mRNAs can be affected through RNase E-mediated co-degradation of the sRNA-mRNA complex (Carrier et al., 2018; Gottesman and Storz, 2011; Wagner and Romby, 2015). Previous biochemical studies suggest two mechanisms for sRNA-mediated degradation: (1) sRNA-mediated reduction of translation leads to a change in degradosome access to the target mRNA, thereby increasing the degradation rate of sRNA-bound mRNA (Arnold et al., 1998; Braun et al., 1998; Prévost et al., 2011; Yarchuk et al., 1992) (here referred to as "passive degradation", or "translation-coupled degradation"), and (2) modulation of degradation through direct recruitment of the degradosome (Bandyra et al., 2012; Massé et al., 2003; Morita et al., 2005; Prévost et al., 2011; Vanderpool and Gottesman, 2004) (here referred to as "active degradation"). For a particular target mRNA, distinct sRNAs may regulate at one or more levels of expression - translation or mRNA stability - by different molecular mechanisms (Carrier et al., 2018; Massé et al., 2003; Vanderpool and Gottesman, 2004; Wagner and Romby, 2015). However, how control at each of these levels quantitatively contributes to the overall regulation efficacy is not well characterized.

One characteristic feature of sRNA regulators is their ability to regulate multiple target mRNAs (Beisel and Storz, 2010; Bobrovskyy et al., 2019; Nitzan et al., 2017; Papenfort and Vogel, 2009). Previous studies have shown that the regulation of various targets by the same sRNA can exhibit a hierarchical pattern; *i.e.* certain targets are more effectively regulated than others (Jost et al., 2013; Levine et al., 2007). Such prioritization in regulation helps optimize stress responses when sRNA abundance is limited (Fang et al., 2016). However, the *in vivo* kinetic determinants that set the regulation hierarchy are largely unclear. A previous *in vivo* kinetic characterization of the sRNA target search and sRNA-mRNA co-degradation processes suggests that the *in vivo* binding affinity between specific sRNA-mRNA pairs can contribute to setting the regulatory hierarchy (Fei et al., 2015), whereas the *in vitro* binding affinity does not seem to correlate with the regulation hierarchy (Bobrovskyy et al., 2019). These observations suggest that *in vivo* target search and regulation kinetics may be collectively determined by complex molecular interactions and kinetic pathways that are difficult to fully recapitulate *in vitro* and therefore require *in vivo* characterization.

In this work, we sought to provide a comprehensive model of sRNA-mediated regulation at the level of translation and mRNA stability. To achieve this goal, we utilized a genetically and biochemically well-characterized *E. coli* sRNA, SgrS, as a model. SgrS is the central regulatory effector of the glucose-phosphate stress response. Intracellular accumulation of phosphorylated

glycolytic intermediates, such as the phosphorylated glucose analog α -methyl glucoside-6-phosphate (α MG6P), along with depletion of other glycolytic intermediates, launches transcription of SgrS, and subsequent regulation of several mRNA targets (Richards et al., 2013). The best characterized targets include negatively regulated *ptsG* mRNA (encoding glucose transporter) (Vanderpool and Gottesman, 2004, 2007), *manXYZ* mRNA (encoding mannose transporter) (Rice and Vanderpool, 2011; Rice et al., 2012), *purR* mRNA (encoding purine biosynthesis operon repressor) (Bobrovskyy and Vanderpool, 2014, 2016), as well as positively regulated *yigL* mRNA (encoding a phosphatase that can dephosphorylate non-metabolizable sugars) (Bobrovskyy and Vanderpool, 2016; Papenfort et al., 2013).

By implementing a combined single-cell imaging and mathematical modeling approach, we determined the kinetic parameters of SgrS regulation of a subset of its target mRNAs. Unexpectedly, our data reveal that instead of acting exclusively on fully synthesized transcripts, SgrS is able to regulate some targets co-transcriptionally. We found that another sRNA, RyhB also acts on nascent mRNA co-transcriptionally, demonstrating that this is a feature of at least two sRNAs previously characterized as post-transcriptional regulators. We find that co-transcriptional regulation by SgrS is attenuated when Rho factor activity is inhibited, indicating that this co-transcriptional regulation is likely due to Rho-dependent termination following sRNA-mediated repression of translation. Finally, our data suggest several important kinetic steps that may determine the efficiency and differential regulation of multiple mRNA targets by an sRNA. Binding of sRNA to the target mRNA is likely the rate-limiting step and may dictate the regulation hierarchy observed within an sRNA regulon. Our approach may be used as a general platform for dissecting kinetic parameters and providing mechanistic details for sRNA-mediated regulation.

Results

Kinetic model and experimental measurement of sRNA-mediated regulation

Since SgrS has been biochemically characterized as a post-transcriptional gene regulator, we first set up a post-transcriptional regulation model to describe this process, including regulation at the levels of both translation and degradation (Figure 1A). In the absence of the sRNA, this model includes basal levels of mRNA transcription (α_m , as rate constant), translation (k_x), and endogenous mRNA and protein degradation (β_m and β_p respectively). When the sRNA is produced, its transcription rate is defined by α_s and the effective degradation rate by β_s . β_s approximates endogenous degradation as well as target-coupled degradation with all other mRNA targets except for the specific target mRNA of interest. The sRNA binds to an mRNA target with an on-rate of k_{on} and dissociates with an off-rate of k_{off} . Upon binding, the translation activity of the bound mRNA changes to k_{xs} . The sRNA-mediated degradation is described by β_{ms} for translation-coupled degradation and β_e for active degradation.

Production of the sRNA, SgrS (from the endogenous chromosomal gene), was induced by exposing *E. coli* cells to glucose-phosphate stress using α-methylglucoside (αMG) under commonly used induction condition (Vanderpool and Gottesman, 2004). The target mRNAs (containing SgrS binding sequences) fused to the super-folder GFP (sfGFP) gene (Pédelacq et al., 2006) were carried on low-copy number plasmids under the control of a tetracycline promoter

(Ptet) (Figure 2A and Table S1). We pre-induced SgrS for 30 minutes before target mRNA induction, and then record time-course changes of SgrS, target mRNA and protein simultaneously upon mRNA induction (defined as time t = 0) (Figure 2B). Fractions of cells were fixed at different time points. SgrS and the target mRNAs were fluorescently labeled through fluorescence in situ hybridization (FISH) (Fei et al., 2015). Translation of the *sfGFP* fusion produced a direct fluorescent readout for protein levels (Figure 2B). The single-cell sRNA, mRNA, and protein levels were characterized by their volume-integrated fluorescent signals (Reyer et al., 2018). sRNA and mRNA copy numbers were further determined through reverse transcription and quantitative PCR (RT-qPCR)-based calibration (Figure 2C and S1). The abundance of endogenous *ptsG* mRNA is 1-2 copies per cell under our growth conditions measured by RT-qPCR, compared to a few hundred copies of the *ptsG-sfGFP* fusion mRNA expressed from the plasmid, suggesting that the contribution of the endogenous mRNAs to our measurement is negligible. As the copy numbers of the RNAs were in the range of tens to hundreds per cell, we described the time-dependent changes in sRNA, mRNA, and protein deterministically by mass action equations (Figure 1B).

We chose to pre-induce the sRNA for two reasons. First, by capturing the sRNA-mediated changes in the production of new proteins, we can more accurately measure regulation at the translational level. sRNA-mediated regulation generally occurs within minutes (Fender et al., 2010; Levine et al., 2007; Vanderpool and Gottesman, 2004). However, many proteins, including the reporter *sfGFP*, have long lifetimes *in E.coli*, which are essentially determined by rate of dilution due to cell division (Maurizi, 1992). Therefore, the fluorescent signal from already existing proteins in the cell can overwhelm any protein level changes caused by sRNAs. Second, and more importantly, we were interested in the timing of sRNA-mediated regulation of target mRNAs and more specifically, whether sRNAs can act on the newly synthesized mRNAs co-transcriptionally. In the case of pre-induced mRNA, the mature mRNAs outcompete the nascent mRNAs owing to their relative abundances, which may make any effect at the transcriptional level undetectable.

For each sRNA-mRNA pair, we measured the time-course changes of sRNA, mRNA and protein levels in four genetic backgrounds: wild-type (WT), $\Delta sgrS$, rme701, and rme701 $\Delta sgrS$. Time-dependent changes in mRNA and protein were recorded in the absence of SgrS for the determination of α_m and k_x of each target mRNA. By comparing the fusion mRNA and protein levels in the $\Delta sgrS$ strain in the presence of αMG with the corresponding levels in the WT strain in the absence of αMG , we noticed that the presence of αMG alone (i.e., without ensuing production of SgrS) reduced the induction of the mRNA fusion (Table S2). One possible explanation for this effect is that the presence of the non-metabolizable αMG stresses the cell and reduces transcriptional activity in general. Therefore, to quantify the regulation by the sRNA specifically, we use the $\Delta sgrS$ and rme701 $\Delta sgrS$ grown in the presence of αMG as our "-sRNA" condition to determine α_m and k_x of the target mRNA in the WT and rme701 backgrounds, respectively.

Comparison of the kinetic behaviors in the WT vs. *rne*701 strain allowed us to separate the effect of sRNA-mediated passive and active degradation. The *me*701 allele encodes a truncated RNase E protein lacking part of the C-terminal unstructured region (Urban and Vogel, 2007), including RhlB, enolase, PNPase and Hfq binding sites (Bandyra et al., 2012, 2018; Hui et al., 2014; Mohanty and Kushner, 2016). The *me*701 mutant still retains its catalytic function but has

an impaired ability to interact with Hfq (Morita et al., 2004, 2005; Urban and Vogel, 2007). Consistent with previous reports (Fei et al., 2015; Sedlyarova et al., 2016), β_m of the fusion mRNAs, measured using rifampicin pulse-chase experiments, did not show any difference between the WT and me mutant background (Figure S2A). This result suggests that me701 has a minor effect on endogenous mRNA degradation, and that accessibility to the translated mRNA is unlikely to be affected by the partial truncation of the C-terminal region of RNase E. Our model therefore assumes that SgrS-mediated mRNA degradation in the me701 background is primarily through translation-coupled degradation.

Finally, additional parameters were experimentally measured to further constrain our model. We measured β_s by first inducing SgrS and then washing away the inducer (Figure S2C). β_s was slightly slower in the me701 background, suggesting that active co-degradation with target mRNAs contributes to the ensemble sRNA turnover, consistent with previous results (Fei et al., 2015). We approximated sfGFP protein half-life using the cell doubling time (~90 min) under our experimental condition (Figure S2D). The six-minute folding time of sfGFP was accounted for in the model by building in a six-minute delay between mRNA and protein production (*i.e.*, the protein present at t = 12 minutes is translated by the mRNA present at t = 6 minutes). α_s was determined by measuring the time-dependent production of SgrS upon induction.

Simulation predicts that SgrS may regulate ptsG co-transcriptionally

Under the assumption that SgrS regulates ptsG-stGFP mRNA post-transcriptionally, we fixed the α_m and k_x values obtained from the $\Delta sgrS$ and rne701 $\Delta sgrS$ strains and fit the rest of the parameters based on the measurements of the WT and me701 strain in the presence of α MG, including β_e , β_{ms} , k_{xs} , k_{on} , and k_{off} . However, the optimized parameters of the post-transcriptional regulation model did not accurately describe the experimental data, specifically the amplitude of sRNA-induced repression (Figure 3A). We therefore considered an alternative model that included the possibility that SgrS could regulate its targets co-transcriptionally, rather than exclusively post-transcriptionally.

Initially, we modeled co-transcriptional regulation by allowing α_m to change in the presence of sRNA (denoted α_{ms}). This model fit the data well (Figure S3A). The resulting α_{ms} (0.87 \pm 0.05 molecules•s⁻¹) was smaller than α_m (1.9 \pm 0.3 molecules•s⁻¹), *i.e.*, transcription was slower in the presence of the sRNA. Since the FISH probes for the target mRNA specifically bind to the sfGFP coding region in the mRNA fusion downstream of the sRNA binding site, we infer that generation of the full-length mRNA, and therefore the fluorescent signal, was reduced upon sRNA binding, or sRNA-mediated regulation may occur during transcription. In addition, the reduction in α_m , was more pronounced in the WT *me* background (α_{ms} = 0.46 α_m) compared to in the *rne*701 background (α_{ms} = 0.98 α_m), suggesting that a fully assembled degradosome contributes to the strength of co-transcriptional regulation.

SgrS decreases the abundance ratio of downstream to upstream regions relative to the SgrS binding site on the target mRNA

Since, according to our model, co-transcriptional regulation by SgrS reduces the production of full-length ptsG-sfGFP mRNA, we reasoned that this may be reflected by a decrease in the abundance of downstream (from the SqrS binding site) relative to upstream regions on the ptsGsfGFP mRNA (henceforth referred to as the "D/U ratio"). To experimentally measure the D/U ratio, we devised a RT-qPCR assay, using two sets of primers: one amplifying the region upstream of the SgrS binding site, and the other amplifying the downstream region (Figure 4A). To evaluate the D/U ratio change specifically contributed by the co-transcriptional regulation, we compared RT-qPCR results on extracted RNA from cells at 1 and 15 min after mRNA induction (Figure 4B). At 1 min after induction (D/ $U_{t=1}$), since the cellular level of mRNA is low (Figure 2C), the fraction of nascent mRNAs, i.e., the mRNAs still being transcribed, compared to fully synthesized mRNAs, should be relatively high. We therefore considered this pool of ptsG-sfGFP mRNAs as relatively enriched in nascent mRNAs and expected that effects at the co-transcriptional level would be enhanced in this sample. At 15 min after induction (D/U_{t=15}), ptsG-sfGFP mRNA levels reach steady-state, with a high cellular abundance (Figure 2C); thus, the fraction of nascent mRNAs should be minimal compared to fully synthesized mRNAs. We therefore reasoned that effects at the co-transcriptional level are largely buried by effects at the post-transcriptional level at this time point.

We measured D/U_{t=1} and D/U_{t=15} in the WT and $\Delta sgrS$ cells in the presence of αMG (Figure 4C). The ratio between the D/U ratios of WT and ΔsgrS cells (reported as "D/U (+/-)" in Figure 4C-E) reflects the change of D/U introduced by SgrS. D/U_{t=15}(+/-) was 0.67±0.18 (mean ± propagated s.d.), suggesting that the regulation by SgrS caused reduction in the abundance of the downstream region compared to the upstream region of the SgrS binding site on the mRNA. The reduced D/U_{t=15} upon SgrS regulation may be explained by the directionality of RNase E activity, i.e., an enhanced RNase E activity on the downstream fragment with 5' monophosphate (Baek et al., 2019; Jiang and Belasco, 2004; Mackie, 1998). In comparison, D/U_{t=1}(+/-) was 0.35±0.03, suggesting that in the nascent-mRNA enriched pool, the regulation by SgrS led to significantly more reduction in the abundance of the downstream region compared to the upstream region, and supporting our prediction that SgrS further repressed the generation of the downstream portion co-transcriptionally. As a control, $D/U_{t=1}(+/-)$ and $D/U_{t=15}(+/-)$ remained around 1 when inducing a non-matching sRNA, RyhB, a small RNA that is produced in response to iron depletion, by adding 2,2'-dipyridyl (referred to as "DIP") into the culture (Figure 4D) (Massé and Gottesman, 2002). In addition, the difference between $D/U_{t=1}(+/-)$ (0.28±0.08) and $D/U_{t=15}(+/-)$ (0.44±0.14) was slightly less in the me701 background (Figure 4C), consistent with the predicted trend from the simulation that the co-transcriptional regulation is stronger in the WT background.

Co-transcriptional regulation by SgrS is dependent on Rho activity

Though co-transcriptional regulation was stronger in WT compared to the *me701* background, it was nonetheless present in both backgrounds. We inferred that RNase E may play a role in co-transcriptional regulation, however, additional factors may contribute. One mechanism that could underlie co-transcriptional regulation is Rho-dependent termination. As SgrS binding to mRNA targets leads to translational repression, reduction in the transcription-coupled translation could lead to increased Rho access to the mRNA followed by premature termination. To test this possibility, we compared the D/U ratios in the presence Bicyclomycin (BCM). BCM targets and

selectively inhibits Rho-dependent transcription termination (Cho et al., 1997; Kohn and Widger, 2005). In the presence of BCM, the significant disparity between $D/U_{t=1}(+/-)$ and $D/U_{t=15}(+/-)$ disappeared, indicating that in the absence of Rho-dependent transcription termination, cotranscriptional regulation is insignificant relative to post-transcriptional regulation (Figure 4E). We therefore conclude that SgrS-induced co-transcriptional regulation of *ptsG-sfGFP* is Rho-dependent.

A revised kinetic model containing co-transcriptional regulation module

After experimentally confirming SgrS-dependent co-transcriptional regulation, we then improved the kinetic model by linking sRNA binding directly to the co-transcriptional regulation (Figure 1C and D). In this revised model, we assumed that sRNA binds and unbinds nascent and mature mRNAs with the same $k_{\rm on}$ and $k_{\rm off}$. In order to allow for co-transcriptional binding, mRNA transcription is separated into two steps: initiation ($k_{\rm ini}$) and elongation ($k_{\rm elon}$). When nascent mRNAs are bound by sRNA during elongation, a free parameter (P) is introduced to the model, representing the probability of generating the full-length, mature mRNA. We allow P to differ between the WT and me701 backgrounds. In addition, we applied the Bayesian information criterion (BIC), where a penalty is applied to the co-transcriptional model for its two added parameters (namely, P, in WT me and me701 background) (Kass and Wasserman, 1995), to select between co-transcriptional and post-transcriptional regulation models. The co-transcriptional model with the lower BIC value was selected, and significantly improved the fitting of data for the SgrS regulation of ptsG-sfGFP (Figure 3B). Consistent with the qPCR results, P was lower in the WT background than in the me701 background (Table S3).

To validate the co-transcriptional regulation model, we generated two data sets. In the first, we reduced the induction of SgrS using a lower concentration of α MG and measured α_s experimentally. In the second, we reversed the induction order of SgrS and ptsG-sfGFP mRNA, presenting the condition under which newly induced sRNAs regulate pre-existing mRNA targets. We simulated the time courses of SgrS, ptsG-sfGFP mRNA, and sfGFP using the best set of parameters obtained from a model with (Figure 5A and B) or without (Figure 5C and D) co-transcriptional regulation, respectively. In both cases, the co-transcriptional regulation model predicted the experimental data better.

Co-transcriptional regulation may be a mechanism utilized by other sRNAs

We next asked if co-transcriptional regulation might be a feature shared by other previously characterized post-transcriptional sRNA regulators. We applied the same imaging and modeling scheme to RyhB and one of its targets, sodB. We generated two fusion mRNAs, $sodB_{130}$ and $sodB_{130+30}$, containing the RyhB binding site and sfGFP gene (Table S1). $sodB_{130+30}$ contains an additional 30 nucleotides which include a RNase E cleavage site and is more sensitive to RyhB regulation at the degradation level (Prévost et al., 2011).

The responses of $sodB_{130}$ and $sodB_{130+30}$ to RyhB regulation were again best captured by the co-transcriptional regulation model (Figures S4 and S5), suggesting that co-transcriptional regulation is not unique to SgrS. Consistent with the SgrS regulation, co-transcriptional regulation

for RyhB was also more efficient in the WT background compared to me701. In addition, the β_e value of the $sodB_{130+30}$ was ~4.5 fold higher than that of the $sodB_{130}$, in line with the addition of the RNase E cleavage site in $sodB_{130+30}$, serving as an additional validation of our model.

Parameters that contribute to regulation efficiency of sRNA over different targets

We next fit the models to two other SgrS targets, *manX* and *purR*. It has been established that *ptsG* is the primary target of SgrS, *manX* is a secondary target, and *purR* is a lower-priority target (Bobrovskyy et al., 2019). Consistently, we observed 78%, 53% and 18% repression respectively for *ptsG*, *manX* and *purR* at the protein level at 24 minutes under the same SgrS induction condition (Table S3). At steady state, the model predicted the regulation efficiency to be 57%, 43% and 5% at the protein level, and 48%, 33% and 11% at the mRNA level for *ptsG*, *manX* and *purR*, respectively. BIC suggested that the co-transcriptional regulation model better fit *manX* (Figure S6), but the post-transcriptional model better fit *purR* (Figure S7), indicating that the contribution of co-transcriptional regulation for *purR* is negligible. Comparison of the parameters for the three mRNA targets for SgrS and two targets for RyhB suggests features that contribute to the overall regulation efficiency (Figure 6A and B, Table S3).

Within the same sRNA regulon, a faster binding rate led to more efficient regulation. We found that k_{on} changed more dramatically than k_{off} among different targets. For SgrS, the difference in k_{off} was within ~2-2.5 fold among the three targets, whereas the change in the k_{on} values was up to ~40 fold between ptsG and purR, suggesting that the binding kinetics is dominated by k_{on} . Interestingly, although $sodB_{130}$ and $sodB_{130+30}$ had the same RyhB target site, which led to the similar k_{off} , $sodB_{130+30}$ showed a higher k_{on} than $sodB_{130}$ (see Discussion). In addition, RyhB had a much higher k_{off} for the sodB constructs compared to SgrS.

The repression at the translation level (k_{xs}/k_x) contributed positively to the regulation efficiency among the SqrS targets. The SqrS binding site is located in the 5' UTR of ptsG mRNA, partially overlapping the RBS, and within the first 10 codons and 34 codons in the coding region of manX and purR respectively (Azam and Vanderpool, 2018; Bobrovskyy and Vanderpool, 2016). SgrS inhibits translation initiation on these mRNAs through different mechanisms. On ptsG mRNA, base pairing of SqrS directly blocks ribosome binding, while on manX and purR mRNAs, binding of SgrS guides Hfg to bind at a site close to the RBS to block ribosome binding (Azam and Vanderpool, 2018; Bobrovskyy and Vanderpool, 2016). Our results indicate that direct binding of SgrS at the RBS may be more efficient in repressing translation, and that the efficiency of translational regulation may decrease as the sRNA binding site moves further into the coding region. k_{xs}/k_x was similar among the two sodB constructs subject to RyhB regulation, consistent with the fact that they share the same RyhB binding site. However, even though RyhB also regulates sodB through directly blocking ribosome binding at the RBS (Geissmann and Touati, 2004; Vecerek et al., 2003), the repression of translation was less efficient than for SgrS regulation of ptsG, suggesting that the different structures of sRNA-mRNA duplexes may affect translation to different extents.

For all target mRNAs, β_{ms} was larger than the corresponding β_{m} , supporting the translation-coupled degradation model in which reduced translation of the sRNA-bound mRNA leads to faster

degradation . For the three SgrS targets, there was no correlation between β_e and regulation efficiency. Although a higher β_e was observed for *purR*, a much smaller k_{on} value for *purR* limited the regulation efficiency, making it the least repressed target of SgrS. The impact of active degradation became more evident when comparing the two RyhB targets, in which most other parameters were similar. The higher β_e value of the $sodB_{130+30}$ contributed to a higher regulation efficiency of $sodB_{130+30}$ (67% and 67% at protein and mRNA levels for $sodB_{130+30}$ respectively compared to 48% and 37% for $sodB_{130}$).

Finally, we observed a positive correlation between the strength of co-transcriptional regulation and the overall regulation efficiency. Co-transcriptionally bound ptsG had a lower probability of generating a full-length mRNA compared to manX, while purR was insignificantly affected by co-transcriptional regulation. Similarly, co-transcriptionally bound $sodB_{130+30}$ had a lower probability of generating a full-length mRNA compared to $sodB_{130}$.

Discussion

We have presented here a general approach combining imaging and modeling, which can be used to quantify the kinetic parameters underlying differential regulation of multiple mRNA targets by a single sRNA. While we focused on mRNAs that are downregulated by their corresponding sRNA, we expect that this approach can easily be adapted to upregulated mRNA targets. In our revised model, SgrS and RyhB can act on nascent transcripts as soon as their binding sites are released from the RNA polymerases (Figure 7A). Further tests on SgrS demonstrate that this cotranscriptional regulation is promoted by Rho-dependent termination, but also affected by the C-terminal region of RNase E. Our model provides the most comprehensive description of sRNA-mediated gene regulation to date and helps dissect kinetic parameters governing hierarchical regulation. We find that binding of SgrS or RyhB to the mRNA target is the rate-limiting step and the primary determinant for setting hierarchical regulation, while regulation at transcription, translation and degradation levels all contribute. Given that SgrS and RyhB are representatives of a large class of base pairing-dependent sRNA regulators, it is possible that similar kinetic behavior may apply to other sRNAs in this class and their regulons.

While our model uses a plasmid-encoded reporter for the target mRNAs, the kinetic parameters we report here should reflect those for endogenous RNAs. Particularly, the degradation rates of the reporter mRNAs and sRNAs are consistent with reported values from previous studies examining endogenous RNAs (Fei et al., 2015). In addition, the $k_{\rm on}$ of SgrS/ptsG-sfGFP and SgrS/manX-sfGFP reported here are within 1-5 fold of the values for SgrS binding to endogenous ptsG and manX mRNAs (Fei et al., 2015). Since the stability of SgrS and RyhB, as well as their target binding are Hfq dependent, the close match between the kinetic parameters measured here and the numbers reported for endogenous RNAs suggests that the plasmid expression of the target mRNAs did not cause Hfq to become a limiting factor. In addition, a recent study reveals that sRNAs can effectively gain access to Hfq even if it is already occupied by mRNAs $in\ vivo$ (Park et al., 2021), further arguing against Hfq becoming the limiting factor in our measurements.

Previous models of sRNA regulation were able to reproduce mRNA repression assuming only post-transcriptional regulation (Arbel-Goren et al., 2013, 2016; Jost et al., 2013; Lavi-Itzkovitz et al., 2014; Levine and Hwa, 2008; Levine et al., 2007; Mehta et al., 2008; Mitarai et al., 2009; Schmiedel et al., 2012). The different order of sRNA and mRNA induction may explain why cotranscriptional regulation has not been noted in previous studies. Previous studies mostly either induced sRNAs in the presence of pre-existing mRNAs, or co-induced mRNAs and sRNAs simultaneously, whereas we pre-induced sRNAs to a certain level before inducing and tracking the changes of targets. Therefore, we created a time window, *i.e.*, early induction phase, when the mature mRNA level was low and the ratio between the nascent mRNA and the mature mRNA was high. Given the high abundance of pre-induced sRNA, and assuming in our model that sRNA used the same binding kinetics for both nascent and mature mRNA targets, the action of sRNA at the co-transcriptional level was enhanced compared to the cases where mature mRNAs were predominant. The effect of co-transcriptional regulation may be further enhanced by the target being plasmid-encoded, as the sRNA may more effectively regulate mRNA co-transcriptionally generated from multiple transcription sites.

While the majority of sRNAs are categorized as post-transcriptional regulators, cases have been reported in which sRNAs can regulate transcription elongation, for example, by modulating the accessibility of the binding site of Rho factor, or by the conformational switch between terminator and antiterminator structures (Brantl et al., 1993; Giangrossi et al., 2010; Novick et al., 1989; Tran et al., 2011). Interestingly, previously characterized post-transcriptional sRNA regulators, DsrA, ArcZ and RprA can also upregulate the target rpoS mRNA by suppressing premature Rho-dependent transcription termination, a mechanism that may be widespread in bacterial genes with long 5' UTRs containing a Rho binding site (Sedlyarova et al., 2016). In addition, ChiX sRNA was observed to co-transcriptionally regulate the distal gene in the chiP cistron by inducing Rho-dependent termination within the chiP coding region, establishing a regulation polarity on the downstream gene within the same cistron (Bossi et al., 2012). More recently, the sRNA OppZ was found to regulate the transcription of oppBCDF mRNA through Rho by inhibiting translation, while having minimal effect on the stability of the transcript (Hoyos et al., 2020). Our results demonstrate, using SgrS and RyhB as examples, that co-transcriptional regulation may be a common feature for sRNAs that can regulate at the translational level, and that regulation on transcription, translation and mRNA degradation by a sRNA can occur simultaneously. While translational repression of the mature mRNAs by sRNAs increases their susceptibility to ribonucleases in the cytoplasm, repression of transcription-coupled translation on the nascent mRNA increases the access of Rho and therefore promotes pre-mature transcription termination. It remains to be demonstrated whether such Rho-dependent co-transcriptional regulation is pervasive throughout sRNA regulons. In addition, our results indicate that the presence of the intact scaffold region of RNase E positively contributes to the co-transcriptional regulation. Future investigation is needed to pinpoint the mechanistic role of RNase E in the cotranscriptional regulation.

Although our target mRNA genes are encoded by plasmids, it is very likely that SgrS and RyhB can act co-transcriptionally on mRNAs produced from the endogenous genes. In order for sRNAs to co-transcriptionally regulate chromosomally encoded targets, sRNAs should be able to diffuse into the nucleoid region. A previous report demonstrated that sRNAs have unbiased

distribution between the nucleoid and cytoplasm using a few plasmid-encoded sRNAs as examples (Fei and Sharma, 2018; Sheng et al., 2017). Here, using single-molecule localization microscopy (SMLM), we confirmed the unbiased localization for endogenously expressed SgrS and RyhB (Figure 7B-E). In addition, the chaperone protein, Hfq, was observed to diffuse freely into the nucleoid region (Park et al., 2021; Persson et al., 2013) and to bind to nascent transcripts (Kambara et al., 2018). It is likely that at least part of the Hfq binding to the nascent transcripts is mediated by sRNAs. For Rho-dependent termination to contribute to co-transcriptional regulation of mRNA targets, Rho utilization (Rut) sites in the endogenous mRNAs must be present. Interestingly, the leader sequences of *ptsG* and *manX* demonstrated sensitivity to BCM treatment in a study by Sedlyarova, et al. (Sedlyarova et al., 2016), consistent with the presence of Rut sites within these endogenous mRNAs. Although the tested targets were not found to contain Rut sites in a recent transcriptome mapping using cells under exponential growth (Adams et al., 2021), it is possible that more Rut sites can be identified in the presence of sRNAs when translation is repressed on the target mRNAs, as in our experimental conditions.

Our model reveals several kinetic steps that can determine the overall regulation efficiency. The binding kinetics between the sRNA and mRNA are the primary determinant of regulation efficiency. While $k_{\rm off}$ differs substantially between different sRNAs, within the regulon of a given sRNA, $k_{\rm on}$ changes more dramatically compared to $k_{\rm off}$, and contributes to setting the regulation priority among different mRNAs. At a constant $k_{\rm on}$, the strength of translational regulation $(k_{\rm xs}/k_{\rm x})$, sRNA-induced RNase E-mediated active degradation $(\beta_{\rm e})$, and regulation efficiency at the cotranscriptional level (P) all positively contribute to the overall regulation efficiency (Figure 6B). However, a $k_{\rm on}$ above 10^5 M⁻¹S⁻¹ is generally needed to repress the target by more than 50% regardless of the rates or efficiencies at other steps (Figure 6B), suggesting that binding of the sRNA to the target mRNA might be the rate-limiting step. This is consistent with the observation that purR, which has a very low $k_{\rm on}$, has the lowest regulation efficiency among SgrS regulon despite a higher $\beta_{\rm e}$.

The in vivo k_{off} value we measured here is of the same order of magnitude compared to the in vitro value using short sRNA-mRNA pair in a recent study (Małecka and Woodson, 2021), suggesting that the restructuring of the target mRNA and abortive annealing of the sRNA-mRNA pair could contribute to the fast sRNA dissociation rate in vivo (Małecka and Woodson, 2021). In addition, other factors in vivo such as competitive ribosome binding may also trigger fast sRNA dissociation. The *in vivo* k_{on} value, on the other hand, is 1-2 orders of magnitude smaller than the in vitro measured value (Małecka and Woodson, 2021). With a k_{on} of 10^5 M⁻¹S⁻¹, it takes a single sRNA ~170 min, and a hundred copies of sRNA ~1.7 min to find a target mRNA. The generally slow binding rates of sRNAs requires high sRNA abundance for efficient gene regulation. The in vivo binding kinetics are not correlated with the in vitro predicted hybridization thermodynamics (Table S1) (Markham and Zuker, 2005), suggesting that more factors in vivo can affect the sRNA target search process. A recent RIL-seg (RNA Interaction by Ligation and sequencing) based study found a positive correlation between the Hfq occupancy of the target mRNA and sRNAtarget interaction frequency, indicating that the binding efficiency of Hfg may affect the sRNA binding kinetics and therefore regulation efficiency of the target mRNA (Faigenbaum-Romm et al., 2020). In addition, the accessibility of the sRNA target site on the mRNA and the requirement for structural rearrangements could also contribute to the differential sRNA binding kinetics among

different targets. Interestingly, when comparing different sRNA-mRNA pairs, we found a positive correlation between k_{on} and the basal translation rate of the mRNA (k_{x}) (Figure 6C), as noted previously (Lavi-Itzkovitz et al., 2014). Specifically, a higher k_{on} observed for $sodB_{130+30}$ compared to $sodB_{130}$ is possibly due to its higher k_{x} . This correlation implies a potential positive role of translating ribosomes in promoting sRNA binding. From a functional point-of-view, it is logical to have a higher regulation efficiency on the most translated targets under stress conditions to achieve the most effective response. One possible mechanism by which the ribosome can facilitate sRNA binding is through unwinding the secondary structures at the sRNA binding site (Hoekzema et al., 2019), while other potential mechanisms are yet to be uncovered.

Finally, assuming an sRNA follows the same binding kinetics for nascent and mature mRNA targets, our model indicates that the relative contributions of regulation at co-transcriptional and post-transcriptional levels depends on the number of potential Rut sites on the mRNA and the relative abundance of nascent and mature mRNAs. Therefore, it is conceivable that during the initial phase of stress, due to the relatively higher abundance of mature mRNAs, the contribution of post-transcriptional regulation might dominate, whereas in the later phase of the stress, when most target mRNAs undergo sRNA-mediated degradation, co-transcriptional regulation might become dominant. This shift of sRNA action from mature mRNAs to newly transcribed mRNAs would be beneficial to achieving timely and efficient regulation upon stress.

Acknowledgements

This work was supported by NIH R01 GM092830. J. F. also acknowledges the support from the Searle Scholars Program, and NIH Director's New Innovator Award (1DP2GM128185-01). A. R. D. acknowledges support from NSF MCB-1953402. We thank Dr. M.S. Azam for useful discussion, MRSEC Shared User Facilities at the University of Chicago for 3D-printing service (NSF DMR-1420709 and DMR-2011854), and the Research Computing Center (RCC) at University of Chicago-operated Midway for providing high-performance computing cluster.

Author contributions

Conceptualization, M.A.R., C.K.V. and J.F;. Methodology, M.A.R. and J.F.; Investigation, M.A.R., E.M.H., X.M. and M.B. Modeling, M.A.R., S.C. and L.H; Writing-Original Draft, M.A.R. and J.F.; Writing-Review & Editing; M.A.R., A.R.D, C.K.V., and J.F.; Funding Acquisition, A.R.D, C.K.V., and J.F.; Supervision, A.R.D, C.K.V., and J.F.

Declaration of interests

The authors declare no competing interests.

Figure legends

Figure 1. Model of sRNA-mediated regulation *in vivo.* (A) Kinetic model describing sRNA-mediated, post-transcriptional regulation. (B) ODE for post-transcriptional regulation model. (C) Kinetic model for co-transcriptional regulation. (D) ODE for co-transcriptional regulation model.

Parameters are described in the text. Dashed blue and red boxes enclose the pathways in the absence and presence of sRNA respectively.

Figure 2. Illustration of experimental setup and representative results. (A) Illustration of the target mRNA, including the SgrS binding site region from the endogenous mRNA target and a coding region for sfGFP reporter. (B) Representative images of SgrS (red), *ptsG-sfGFP* mRNA (green) and sfGFP signal (blue) in the absence (upper) or presence (lower) of sRNA induction. (C) Measured sRNA, mRNA, and protein levels from images in (B). Points with error bars represent standard deviation (s.d.) from 2-3 biological replicates, with each replicate containing ~500-1000 cells.

Figure 3. Fitting of SgrS regulation of *ptsG* expression with post-transcriptional and cotranscriptional regulation models. Time-dependent changes of SgrS, *ptsG-sfGFP* mRNA, and sfGFP levels in the presence or absence of SgrS, and in the WT *rne* background or *rne*701 background, fit with (A) post-transcriptional regulation model using one-step transcription module, or (B) co-transcriptional regulation model with two-step transcription module. Points with error bars represent s.d. of experimental data from 2-3 biological replicates, each containing ~500-1000 cells. Black lines represent best fits. Shaded, colored regions represent predicted error of the fitting, calculated by sampling one hundred sets of kinetic parameters from the posterior distribution and plotting the associated curves over the observed data.

Figure 4. RT-qPCR measurement of the D/U ratio. (A) Schematic illustration of the qPCR primer binding sites relative to SgrS binding site on the mRNA. (B) Schematic illustration of total RNAs extracted at different time points of mRNA induction, which contain different ratios of nascent mRNAs to fully transcribed mRNAs. (C) Reduction in the D/U ratio of ptsG-sfGFP mRNA affected by SgrS (D/U(+/-), defined by the ratio of D/U(+) (in the presence of SgrS) to D/U(-) (in the absence of the SgrS). (D) D/U(+/-) of ptsG-sfGFP mRNA is unaffected by RyhB. (E) D/U(+/-) of ptsG-sfGFP mRNA affected by SgrS with addition of Bicyclomycin (BCM). 50 µg/mL BCM was added 15 minutes before the time of cell collection, i.e. at t = -14 min relative to mRNA induction for cells collected at t=1 min, and t = 0 relative to mRNA induction for cells collected at t = 15 min. For each data set, the s,d, of D/U(-) and D/U(+) were calculated respectively from 3-8 biological replicates. The reported error bars for D/U(+/-) were propagated s.d., calculated using standard error propagation formulas. Significance values from two-sample t-tests are reported above error bars.

Figure 5. Co-transcriptional regulation model outperforms the co-transcriptional model in predicting the kinetics of sRNA regulation. (A) Simulated prediction (black curve with shaded, colored region) using co-transcriptional regulation model for validation dataset with (A) reduced α MG concentration for SgrS induction, and (B) pre-induced mRNA, overlaid with experimental data (points with error bars representing s,d, from 2-3 biological replicates, each containing ~500-1000 cells). Simulated prediction using post-transcriptional regulation model for validation dataset with (C) reduced α MG concentration for SgrS induction, and (D) pre-induced mRNA.

Figure 6. Kinetic parameters that contribute to regulation efficiency of sRNA over different targets. (A) Parameters of sRNA regulation over different mRNA targets. Error bars represents

s.d. from 2-3 biological replicates, each containing ~500-1000 cells. p-values for two-sample t-tests are provided for pairwise comparisons. * indicates p<0.0001. (B) Protein-level repression heatmap, calculated by screening across the listed parameters. Repression level of 1 represents complete repression of protein expression; 0 means no repression. For the left panel, $\beta_e = 1.0 \times 10^{-3} \text{ S}^{-1}$, and P = 0.32. For middle panel, $k_{xs}/k_x = 0.5$ and P = 0.32. For right panel, $k_{xs}/k_x = 0.5$ and $\beta_e = 1.0 \times 10^{-3} \text{ S}^{-1}$. For all simulations, k_{init} , k_x , k_{off} , β_m , β_m , β_s , and α_s are set to the measured or MAP values for ptsG (Tables S2 and S3). (C) k_{on} vs. k_x for all mRNA targets. Error bars represent s,d of calculated MAP values (Table S2 and S3).

Figure 7. Model for co-transcriptional regulation by sRNAs. (A) sRNAs can freely diffuse in into the nucleoid region of bacterial cells and bind to the target mRNAs as soon as the sRNA binding site is transcribed. Binding of sRNA affect transcriptional-coupled translation and increase the binding of Rho, thereby terminating transcription. Recruitment of RNase E through its C-terminal scaffold region positively contributes to the efficiency of co-transcriptional regulation. Representative SMLM images of SgrS in the absence of ptsG-sfGFP mRNA induction (30 min after sRNA induction, before mRNA induced) (B), and in the presence ptsG-sfGFP mRNA induction (54 min after sRNA induction, 24 min after mRNA induction) (C). Representative SMLM images of RyhB in the absence (D) and presence (E) of $sodB_{130}$ -sfGFP induction. Red spots are sRNA signals detected by SMLM imaging. Blue area represents DAPI-stained nucleoid region. (F) Enrichment of for SgrS and RyhB in the absence and presence of the target mRNA in the nucleoid and cytoplasm regions. Error bars represents s.d. from 2-3 biological replicates, each containing ~100 cells.

STAR Materials and methods

RESOURCE AVAILABILITY

Lead contact

Further information and requests for resources and reagents should be directed to and will be fulfilled by the lead contact, Jingyi Fei (<u>jingyifei@uchicago.edu</u>).

Materials availability

All strains and plasmids in this study are available from the lead contact upon request.

Data and code availability

- All data has been deposited at Mendeley Data and are publicly available as of the date
 of publication. The DOIs are listed in the key resources table.
- All original code has been deposited at Zenodo and is publicly available as of the date of publication. DOIs are listed in the key resource table.
- Any additional information required to reanalyze the data reported in this paper is available from the lead contact upon request.

EXPERIMENTAL MODEL AND SUBJECT DETAILS

Bacterial strains, plasmids

DB166 was made via P1 transduction by moving *laclq*, *tetR*, *specR* cassette from JH111 (Rice and Vanderpool, 2011) into DJ480. Δ*ryhB::cat* was moved to DB166 from EM1453 (Jacques et al., 2006) via P1 transduction to create DB186. *me701-FLAG-cat* was moved into strains DB166 and JH111 (Rice and Vanderpool, 2011) by P1 transduction from TM528 (Morita et al., 2004) to create XM100 and XM101 respectively. The *ryhB::tet* allele in strain XM221 was created by using primers OXM211 and OXM212 with homology to RyhB to amplify the tetracycline resistance cassette. The PCR product was recombined into the chromosome of XM100 using λ red functions provided by pSIM6 (Datta et al., 2006).

All cell strains used in this work are listed in Key Resources Table, and primers used for PCR are listed in Supplementary Table S5.

METHOD DETAILS

Plasmid construction

Target mRNAs are all encoded by pSMART plasmid and under P_{tet} promoter. Target mRNA reporters carry the small RNA binding sequence from the endogenous mRNAs, and a *sfGFP* gene (Supplementary Table S1). pSMART *ptsG*-10aa-*sfGFP* ("10aa" refers to the first 10 codons) was

generated from pZEMB8 (Bobrovskyy et al., 2019) using site directed mutagenesis and the pSMART LCKan Blunt Cloning Kit (Lucigen, 40821-2). Briefly, the lac promoter of pZEMB8 was switched to a tet promoter to reduce leaky expression, using primers (JZ25 and JZ26) that include 5' overhangs containing the tetracycline promoter sequence. The fragment containing the entire promoter, gene of interest, and terminator was generated by PCR using primers EH1 and EH2 and ligated into the pSMART vector, following manufacturer's instructions. pSMART manX-34aa sfGFP was generated following the same method as pSMART ptsG-10aa sfGFP, with pZEMB10 (Bobrovskyy and Vanderpool, 2016) serving as the template for the manX-34aa-sfGFP region, and primers JZ26 and EH3 containing the tetracycline promoter sequence. pSMART ptsG-10aa-sfGFP was further used to generate pSMART purR-32aa-sfGFP and pSMART sodB₄₃₀-sfGFP using Gibson Assembly. sodB₄₃₀ contains RyhB binding site on sodB mRNA and additional 363 nucleotides in the coding region. pSMART sodB₁₃₀-sfGFP and pSMART sodB₁₃₀₊₃₀-sfGFP were generated from pSMART sodB₄₃₀-sfGFP by using primers (EH390/EH391 and EH440/441) that amplify the entire plasmid, excluding the regions that were not desired in sodB₁₃₀-sfGFP or sodB₁₃₀₊₃₀-sfGFP. The PCR products were then phosphorylated (NEB M0201S) and ligated (NEB M0202S) before transformation. Each plasmid was confirmed by DNA sequencing and transformed into the various genetic backgrounds utilized in this study.

All plasmids used in this work are listed in Key Resources Table, and primers used for PCR are listed in Supplementary Table S5.

Culture growth and induction for imaging

For all imaging and qPCR experiments, overnight *E. coli* cultures were grown in LB media with 25 ug/mL Kanamycin. Overnight cultures were diluted 100-fold in MOPS-Minimal media (TEKnova, M2106) supplemented with 1% glycerol and 25 μ g/mL kanamycin at 37 °C. The cells were grown to approximately OD = 0.2-0.3, at which point SgrS or RyhB was induced by adding 0.5% α MG or 500 μ M DIP directly to the culture. The stress was present for 30 minutes before induction of the reporter mRNA construct using 10 ng/mL anhydrous tetracycline (aTc, Sigma-Aldrich). The time of aTc induction marked the t=0 time point in imaging experiments. Fractions of cells were taken at different time points after mRNA induction for downstream sample treatment.

Fluorescence in situ hybridization (FISH)

10 FISH probes targeting the sfGFP coding region, 9 probes for SgrS and 4 probes for RyhB were designed using the Stellaris Probe Designer from Biosearch, and labeled as previously described (Fei et al., 2015). sfGFP probes were labeled Alexa Fluor 568 NHS ester (A568, Invitrogen A20003). SgrS and RyhB probes were labeled with Alexa Fluor 647 NHS ester (A647, Invitrogen A20006). The 16S rRNA probe was labeled with Alexa Fluor 405 NHS ester (A405, Invitrogen A30000). The A405 signal serves to indicate sufficient permeabilization. FISH was performed as previously described (Fei et al., 2015). 10 mL of culture of cells were taken out at the corresponding time points and fixed with 4% formaldehyde at room temperature (RT) for 30 minutes. Cells were then permeabilized with 70% ethanol for 1 hour at RT. After ethanol permeabilization, 60 μ L samples were taken for each time point and cells were additionally permeabilized with 25 μ g/mL lysozyme for 10 minutes (1 μ g/mL lysozyme corresponds to 70 units/mL). Cells were hybridized with labeled DNA probes (Supplementary Table S5) in the FISH

Hybridization buffer (10% dextran sulfate (Sigma D8906) and 10% formamide in 2x SSC) at 30° C in the dark for overnight. The concentration of the labeled probes was 15 nM per probe for mRNAs, 50 nM per probe for sRNAs, and 10 nM for 16S rRNA. After the hybridization, samples were washed three times with 10% formamide in 2x SSC and resuspended in 4x SSC.

Epi-fluorescence Imaging and image analysis

Cells in 4x SSC buffer were imaged in 3D printed 2-well chambers. 1.2-1.4 μ L of the sample were placed on the glass slide bottom of the chamber, with a 1% agarose gel pad placed on top to lay the cells flat. Imaging was performed on a custom inverted microscope (Nikon Ti-E with 100x NA 1.49 CFI HP TIRF oil immersion objective) (Park et al., 2018). Multicolor Z-stack images were taken with 0.130 μ m step size and 11 slices for each color. SgrS-A647 and RyhB-A647, mRNA-A568, sfGFP, and 16S rRNA-A405 were imaged with a 647 nm laser (Cobolt 06-01), a 561 nm laser (Coherent Obis LS), a 488 nm laser (Cobolt 06-01), and a 405 nm laser (CrystaLaser, DL405-025-O), respectively. In addition to the multicolor z-stack images, each image had a corresponding differential interference contrast (DIC) image, used for segmentation and image analysis purposes.

Cells were segmented individually based on DIC images using homemade MATLAB code (Reyer et al., 2018). The segmented cell mask was then overlaid on each color channel stack individually, and the volume-integrated fluorescence intensity was calculated by adding the areaintegrated intensities of each cell for the 5 most in-focus slices (the most in-focus slice, and two slices above and below). The background intensities of the image and of the cells due to nonspecific binding of the FISH probes were subtracted from the calculated volume-integrated intensities. The signal contributed by probe nonspecific binding was measured using the same imaging conditions by calculating the volume integrated intensities of cells lacking target RNAs but in the presence of the FISH probes at the same concentration as for positive samples. ΔsqrS cells (JH111) without transformation of any mRNA-sfGFP fusion plasmids were used for background measurements in the sRNA, mRNA, and GFP channels. The 16S rRNA-A405 signal was used as an indicator of sufficiently permeabilized and labeled cells. Background A405 fluorescence intensity distribution due to probe nonspecific binding was first determined using cells labeled with the same concentration of off-target A405-labeled probes. A threshold at the 90th percentile of the background intensity distribution was then used as the 405 intensity cutoff. Cells with 16S rRNA -A405 intensities below this threshold (less than 10% of the total population) were considered not sufficiently permeabilized, and not included in further analysis.

SMLM Imaging and image analysis

Single molecule localization microscopy (SMLM) imaging was conducted using the same microscope as described above with super-resolution modality (Park et al., 2018). Fixed cells were immobilized on the 8-well chambered glass coverslip (Cellvis C8-11.5H-N) using poly-L-lysine (Sigma-Aldrich P8920) and imaged in imaging buffer (50 mM Tris-HCl, 10% glucose,1% 2-Mercapgtoethanol (Sigma-Aldrich M6250), 50 U/mL glucose oxidase (Sigma Aldrich G2133-10KU), 404 U/mL catalase (EMD Millipore 219001) in 2X SSC, pH = 8.0). Images were acquired through a custom programmed data acquisition code, which programs the laser power, camera

exposure time, and spot detection threshold, using the Nikon NIS JOBS function. SMLM images were reconstructed with the IDL analysis package as previously published (Park et al., 2018).

RT and qPCR

Total RNA was extracted from each sample using Trizol (Thermo Fisher, 15596026) extraction. 2 mL culture of bacterial cells were collected at the desired time point and immediately spun at 12,000 g for 1 minute in cold. The cell pellet was homogenized in 200 μ L of trizol incubated at RT for 5 minutes. 1/5 volume of chloroform was added to the Trizol mixture. After incubation for 2-5 minutes at RT, the mixture was centrifuged at 12,000 g for 5 minutes. The upper phase was transferred to a new tube and extracted again with chloroform. The aqueous layer was collected, from which the RNA was then precipitated by standard ethanol precipitation. The total RNA pellet is resuspended in nuclease-free water, and further desalted by a P6 microspin column (Bio-Rad, 7326221). Genomic DNA contamination in the total RNA was further removed by DNase treatment. 2 μ L of Turbo DNase (Thermo Fisher, AM2238) was added to 2 μ g of total RNA, and the reaction was incubated for 2 hours at 37° C. The DNase was inactivated by adding EDTA (pH = 8) at a final concentration of 15 mM and incubating at 75° C for 10 minutes. The reaction was desalted by a P6 column.

Each reverse transcription (RT) reaction was performed using 50 ng total RNA in 1 mM dNTPs (NEB N0447S), 10% DMSO (Fisher, BP231), 10 mM DTT (Sigma-Aldrich, 10197777001), 250 nM of gene specific reverse primer (IDT), and 20-fold dilution of reverse transcriptase from iScript cDNA Synthesis Kit (Bio-Rad, 1708891) and incubated following manufacturer instructions. Each qPCR reaction was prepared using 1X SsoAdvanced Universal SYBR Green Supermix (Bio-Rad 1725274), 250 nM forward and reverse primers (Supplementary Table S5), and 1 μ L of cDNA generated by the RT reaction in a final volume of 20 μ L. The qPCR reactions were performed with CFX real-time PCR system (Bio-Rad), using pre-incubation of 95 °C for 30 s, followed by 40 cycles of 95 °C for 10 s and 60 °C for 30 s. The reported D/U ratio (R_{D/U}), a ratio between the downstream and upstream amplification of the mRNA target, was calculated as:

$$R_{D/U} = \frac{1}{2^{(Ct_D - Ct_U)}}$$

where Ct_D and Ct_U are the Ct values of the downstream and upstream amplicons respectively.

Determination of sRNA and mRNA copy numbers

To convert the mRNA and sRNA fluorescence values to molecule copy numbers, a qPCR calibration curve of RNA copy number vs. Ct value was first built. *ptsG-sfGFP* mRNA and SgrS were produced using *in vitro* transcription. PCR using forward primers harboring the T7 promoter sequence were used to produce linear dsDNA transcription templates (Supplementary Table S5) and 1 µg template was incubated in T7 buffer (160 mM HEPES-KOH, pH 7.5, 20 mM DTT, 3 mM each rNTP, 20 mM MgCl₂, 2 mM spermidine, 120 unites SUPERase In RNAse inhibitor) and 10 units T7 RNA polymerase (kind gift from Yuen-Ling Chan) at 37 °C for overnight. 4 units TURBO DNase was added to remove template DNA and incubated at 37 °C for an additional 2 hours. RNA was extracted using standard phenol-chloroform and confirmed on a 7% Urea-PAGE gel.

To build a calibration curve between Ct value and RNA copy number, RT reactions were performed on a series of dilutions of *in vitro* transcribed RNA, from 10 ng to 0.001 ng. Different amounts of *in vitro* transcribed RNA were spiked into collected cell samples, then subjected to the same total RNA extraction protocol as described above. Briefly, *JH111* cells ($\Delta sgrS$ cells with the plasmid encoding the mRNA-sfGFP) were grown under the same conditions used for imaging and collected when cells reached $OD_{600} = 0.2$ -0.3. Cells were spun down, then homogenized in Trizol. At this point (after adding Trizol, but before subsequently spinning down and adding chloroform) the *in vitro* transcribed RNA was added. RT was performed using iScript cDNA Synthesis Kit (Bio-Rad, 1708891) and qPCR was performed using SsoAdvanced Universal SYBR Green Supermix (Bio-Rad 1725274). A linear function was fit between the Ct values of the qPCR reactions and the logarithm of the input RNA copy numbers (Figure S1A). The copy number of the RNA was calculated using the known molecular weight of the RNA and the amount of RNA added to the initial RT reaction.

To relate RNA copy number and arbitrary fluorescence values, cell samples with different RNA expression levels were subjected to RNA extraction, RT-qPCR, and fluorescence measurement, as described above. Based on the Ct value vs. RNA copy number calibration curve built above, sfGFP fusion mRNA and SgrS copy numbers were calculated for the extracted RNA of each sample, and further converted into copy number per cell based on the cell numbers measured by OD₆₀₀ for each sample. RNA copy number per cell was then plotted against the volume-integrated cell fluorescent intensities for each corresponding sample and fit with a linear function (Figure S1B). Fluorescent intensities of the cells from the imaging experiments were compared to this calibration curve of fluorescent intensity vs. RNA copy number to extract RNA copy number per cell. For RyhB, the conversion factor between SgrS fluorescence values and copy number was multiplied by 4/9, as only 4 FISH probes were used to label RyhB compared to 9 for SgrS, which was used to create the calibration curve. We assume a linear relationship between number of probes and fluorescent intensity.

Simulation, fitting, and model selection

We used Markov Chain Monte Carlo (MCMC) simulation to explore the parameter spaces of our kinetic models as defined by their ordinary differential equations (ODEs). Specifically, we utilized the *emcee* package (Foreman-Mackey et al., 2013), which is a Python implementation of the Goodman-Weare Affine Invariant Ensemble Sampler (Goodman and Weare, 2010), and integrated the ODEs with the LSODA solver (Petzold, 1983; Virtanen et al., 2020). In this approach, an ensemble of parameter sets evolves to sample a Bayesian posterior distribution, which is the product of a prior distribution and a likelihood function. Assuming Gaussian and independent errors, the logarithm of the likelihood (log-likelihood) function takes the form:

$$L = \ln p(y|x,\theta) = \sum_{m} \left\{ -\frac{1}{2} \sum_{n} \left[\frac{(y_{m,n} - f(x_{m,n}|\theta))^2}{\sigma_{m,n}^2} \right] \right\},$$

where m is the molecular species (mRNA, sRNA, and protein in the WT and me701 strain, for a total of 6), n is the time point (7 in our case, t = 0, 1, 3, 6, 12, 18 and 24 min), $y_{m,n}$ is the experimental value for molecular species m at time t_n , (in units of copy number for sRNA and mRNA, and arbitrary fluorescent unit for protein), $f(x_{m,n}|\theta)$ is the simulated value for molecular species m at time t_n given the parameter value set θ , $\sigma_{m,n}^2$ is the experimental variance for molecular species m at time point t_n . The six-minute folding time of sfGFP is directly accounted for in the fitting process by introducing a six minute time delay in protein observation, meaning that the protein fluorescent signal is assumed to have been produced by mRNA transcribed six minutes earlier (e.g. $y_{\text{WT-Protein},t=12}$ corresponds to $y_{\text{WT-mRNA},t=6}$). The log-posterior distribution is the sum of the log-prior distribution and log-likelihood function.

We fit parameters by running simulations in a two-step process. First, mRNA transcription and translation rates were fit using the -sRNA experimental data, i.e. the data acquired from the cell samples in the absence of sRNA. The best fit parameter values and their associated errors were used as prior distributions for transcription and translation rates in the second step, where the rest of the parameters were determined by fitting to the +sRNA experimental data, acquired from cell samples in the presence of sRNA. For the co-transcriptional regulation model using the one-step transcription module, the –sRNA simulations explored a 3-dimensional parameter space: $[\alpha_m, k_x, \beta_m]$; and the +sRNA simulations explored a 9-dimensional parameter space: $[k_{on}, k_{off}, k_{xr}, k_{off}, k_{xr}]$ $\beta_{\rm e}$, $\beta_{\rm ms}$, $k_{\rm x_wt}$, $k_{\rm x_rne}$, $\alpha_{\rm ms_wt}$, $\alpha_{\rm ms_rne}$], where $k_{\rm xr}$ is the ratio $k_{\rm xs}/k_{\rm x}$. For the post-transcriptional regulation model using the one-step transcription module, α_{ms_wt} and α_{ms_rne} were set to α_{m_wt} and $\alpha_{\rm m}$ me, respectively. For the co-transcriptional regulation model using the two-step transcription module, the –sRNA simulations explored a 3-dimensional space: $[k_{init}, k_x, \beta_m]$. The elongation rate, kelon was assumed to be a constant for each mRNA, determined by dividing a constant elongation speed (50 nucleotides per second (Young and Bremer, 1976)) by the length of the mRNA. The +sRNA simulations explored a 9-dimensional space [k_{on} , k_{off} , k_{xr} , β_e , β_{ms} , k_x wt, k_x rne, P_{wt} , P_{rne}], where $P_{\rm wt}$ and $P_{\rm rne}$ represent the probability of generating full length mRNA in WT rne and rne701 backgrounds, respectively. For the post-transcriptional regulation model using the two-step transcription module, P_{wt} and P_{me} were set to 1. For -sRNA simulations in 3 dimensions, 50 walkers, representing 50 parameter sets, each evolved for 10000 steps, which we found to be a sufficient number of steps for the log posterior to level off. For +sRNA simulations in 9 dimensions, 100 walkers each evolved for 10000 steps. Initial positions for the walkers were chosen at random from the bounded interval of possible values defined by its prior distribution. We used the default settings for the emcee sampler, such that the each move is a "stretch" move, with stretch parameter, a = 2, giving an average acceptance fraction equal to 0.44 (Foreman-Mackey et al., 2013; Goodman and Weare, 2010).

For –sRNA fitting, the prior distributions for the free parameters were uniform distributions (Table S4). For the +sRNA fitting, the prior distributions of the parameters determined from the – sRNA fitting were normal distributions centered on their –sRNA maximum a posteriori (MAP) values, and the prior distributions for the remaining parameters were uniform distributions. After the parameter fitting, the posterior probability distributions of the fitted parameters were determined, along with their MAP values and associated errors. For experimentally determined variables, the widths of the normal distributions were determined by their experimental errors. For

the remaining free parameters, the widths of the uniform distributions were set empirically, either by observing physical constraints (e.g., k_{on} is constrained by the diffusion limit) or by logical constraints (e.g., k_{xr} cannot be below 0 or above k_x).

Each experimental replicate was fit separately. $\sigma_{m,n}^2$ was the same across all replicates. A single set of parameter values was chosen to be the best fit for the combined samples by selecting the point estimate of the MAP parameter values for the best walker for each replicate, then averaging over the replicates. One replicate in a –sRNA simulation was one experimental dataset containing mRNA and associated protein values, with datasets for WT and me701 backgrounds fit separately. One replicate in a +sRNA simulation was a combination of one experimental dataset in the WT background, and one in the me701 background. The reported parameter values and their associated errors were the mean and standard deviations of the MAP values from all simulations, respectively. All simulations were performed with custom software written in Python, and parallelization was implemented using emcee. We utilize both CPU and GPU functions to maximize the efficiency of our simulations. All codes for all simulations are available publicly on GitHub: (https://github.com/JingyiFeiLab/Regulation Kinetics).

The Bayesian information criterion (BIC) was used for model selection between post-transcriptional and co-transcriptional regulation models. The BIC is defined as:

$$BIC = k \ln(n) - 2\ln(\hat{L})$$

where \hat{L} is the maximized likelihood value of the model, k is the number of parameters (k = 7 for post-transcriptional model, k = 9 for co-transcriptional model, accounting for the added variables P_{wt} and P_{me}), n is the number of data points or observations (n = 42 in our case, representing 7 time points x 3 molecules x 2 me backgrounds). For each target, the minimized BIC was calculated for both the post- and co-transcriptional models, and the model which produced the lowest BIC was selected.

QUANTIFICATION AND STATISTICAL ANALYSIS

All imaging data was quantified by custom written MATLAB code. The significance values reported in Figures 4 and 6 were calculated by two sampled t-tests. Statistical details are found in the figure legends.

Supplemental Information

Table S5. List of all oligonucleotides used in this study. Related to STAR Methods

References

Adams, P.P., Baniulyte, G., Esnault, C., Chegireddy, K., Singh, N., Monge, M., Dale, R.K., Storz, G., and Wade, J.T. (2021). Regulatory roles of Escherichia coli 5' UTR and ORF-internal RNAs detected by 3' end mapping. Elife *10*.

Arbel-Goren, R., Tal, A., Friedlander, T., Meshner, S., Costantino, N., Court, D.L., and Stavans,

J. (2013). Effects of post-transcriptional regulation on phenotypic noise in Escherichia coli. Nucleic Acids Res. *41*, 4825–4834.

Arbel-Goren, R., Tal, A., Parasar, B., Dym, A., Costantino, N., Muñoz-García, J., Court, D.L., and Stavans, J. (2016). Transcript degradation and noise of small RNA-controlled genes in a switch activated network in Escherichia coli. Nucleic Acids Res. *44*, 6707–6720.

Arnold, T.E., Yu, J., and Belasco, J.G. (1998). mRNA stabilization by the ompA 5' untranslated region: two protective elements hinder distinct pathways for mRNA degradation. RNA 4, 319–330.

Azam, M.S., and Vanderpool, C.K. (2018). Translational regulation by bacterial small RNAs via an unusual Hfq-dependent mechanism. Nucleic Acids Res. *46*, 2585–2599.

Baek, Y.M., Jang, K.-J., Lee, H., Yoon, S., Baek, A., Lee, K., and Kim, D.-E. (2019). The bacterial endoribonuclease RNase E can cleave RNA in the absence of the RNA chaperone Hfq. J. Biol. Chem. *294*, 16465–16478.

Bandyra, K.J., Said, N., Pfeiffer, V., Górna, M.W., Vogel, J., and Luisi, B.F. (2012). The seed region of a small RNA drives the controlled destruction of the target mRNA by the endoribonuclease RNase E. Mol. Cell *47*, 943–953.

Bandyra, K.J., Wandzik, J.M., and Luisi, B.F. (2018). Substrate recognition and autoinhibition in the central ribonuclease rnase E. Mol. Cell *72*, 275–285.e4.

Beisel, C.L., and Storz, G. (2010). Base pairing small RNAs and their roles in global regulatory networks. FEMS Microbiol. Rev. *34*, 866–882.

Bobrovskyy, M., and Vanderpool, C.K. (2014). The small RNA SgrS: roles in metabolism and pathogenesis of enteric bacteria. Front. Cell Infect. Microbiol. *4*, 61.

Bobrovskyy, M., and Vanderpool, C.K. (2016). Diverse mechanisms of post-transcriptional repression by the small RNA regulator of glucose-phosphate stress. Mol. Microbiol. 99, 254–273.

Bobrovskyy, M., Azam, M.S., Frandsen, J.K., Zhang, J., Poddar, A., Ma, X., Henkin, T.M., Ha, T., and Vanderpool, C.K. (2019). Determinants of target prioritization and regulatory hierarchy for the bacterial small RNA SqrS. Mol. Microbiol. *112*, 1199–1218.

Bossi, L., Schwartz, A., Guillemardet, B., Boudvillain, M., and Figueroa-Bossi, N. (2012). A role for Rho-dependent polarity in gene regulation by a noncoding small RNA. Genes Dev. *26*, 1864–1873.

Brantl, S., Birch-Hirschfeld, E., and Behnke, D. (1993). RepR protein expression on plasmid pIP501 is controlled by an antisense RNA-mediated transcription attenuation mechanism. J. Bacteriol. *175*, 4052–4061.

Braun, F., Le Derout, J., and Régnier, P. (1998). Ribosomes inhibit an RNase E cleavage which induces the decay of the rpsO mRNA of Escherichia coli. EMBO J. 17, 4790–4797.

Caldelari, I., Chao, Y., Romby, P., and Vogel, J. (2013). RNA-mediated regulation in pathogenic bacteria. Cold Spring Harb. Perspect. Med. *3*, a010298.

Carrier, M.-C., Lalaouna, D., and Massé, E. (2018). Broadening the definition of bacterial small rnas: characteristics and mechanisms of action. Annu. Rev. Microbiol. 72, 141–161.

Cho, H., Park, H., Zhang, X., Riba, I., Gaskell, S.J., Widger, W.R., and Kohn, H. (1997). Design, Syntheses, and Evaluations of Bicyclomycin-Based Rho Inactivators. J. Org. Chem. *62*, 5432–5440.

Datta, S., Costantino, N., and Court, D.L. (2006). A set of recombineering plasmids for gram-

negative bacteria. Gene 379, 109-115.

Faigenbaum-Romm, R., Reich, A., Gatt, Y.E., Barsheshet, M., Argaman, L., and Margalit, H. (2020). Hierarchy in hfq chaperon occupancy of small RNA targets plays a major role in their regulation. Cell Rep. *30*, 3127–3138.e6.

Fang, F.C., Frawley, E.R., Tapscott, T., and Vázquez-Torres, A. (2016). Bacterial Stress Responses during Host Infection. Cell Host Microbe *20*, 133–143.

Fei, J., and Sharma, C.M. (2018). RNA localization in bacteria. Microbiol. Spectr. 6.

Fei, J., Singh, D., Zhang, Q., Park, S., Balasubramanian, D., Golding, I., Vanderpool, C.K., and Ha, T. (2015). RNA biochemistry. Determination of in vivo target search kinetics of regulatory noncoding RNA. Science *347*, 1371–1374.

Felden, B., and Cattoir, V. (2018). Bacterial Adaptation to Antibiotics through Regulatory RNAs. Antimicrob. Agents Chemother. *62*.

Fender, A., Elf, J., Hampel, K., Zimmermann, B., and Wagner, E.G.H. (2010). RNAs actively cycle on the Sm-like protein Hfq. Genes Dev. *24*, 2621–2626.

Foreman-Mackey, D., Hogg, D.W., Lang, D., and Goodman, J. (2013). emcee: the MCMC hammer. PUBL. ASTRON. SOC. PAC. *125*, 306–312.

Geissmann, T.A., and Touati, D. (2004). Hfq, a new chaperoning role: binding to messenger RNA determines access for small RNA regulator. EMBO J. 23, 396–405.

Gerdes, K., and Wagner, E.G.H. (2007). RNA antitoxins. Curr. Opin. Microbiol. *10*, 117–124. Giangrossi, M., Prosseda, G., Tran, C.N., Brandi, A., Colonna, B., and Falconi, M. (2010). A novel antisense RNA regulates at transcriptional level the virulence gene icsA of Shigella flexneri. Nucleic Acids Res. *38*, 3362–3375.

Goodman, J., and Weare, J. (2010). Ensemble samplers with affine invariance. Comm. App. Math. Comp. Sci. *5*, 65–80.

Gottesman, S., and Storz, G. (2011). Bacterial small RNA regulators: versatile roles and rapidly evolving variations. Cold Spring Harb. Perspect. Biol. 3.

Hoekzema, M., Romilly, C., Holmqvist, E., and Wagner, E.G.H. (2019). Hfq-dependent mRNA unfolding promotes sRNA-based inhibition of translation. EMBO J. 38.

Holmqvist, E., and Wagner, E.G.H. (2017). Impact of bacterial sRNAs in stress responses. Biochem. Soc. Trans. *45*, 1203–1212.

Hoyos, M., Huber, M., Förstner, K.U., and Papenfort, K. (2020). Gene autoregulation by 3' UTR-derived bacterial small RNAs. Elife 9.

Hui, M.P., Foley, P.L., and Belasco, J.G. (2014). Messenger RNA degradation in bacterial cells. Annu. Rev. Genet. 48, 537–559.

Jacques, J.-F., Jang, S., Prévost, K., Desnoyers, G., Desmarais, M., Imlay, J., and Massé, E. (2006). RyhB small RNA modulates the free intracellular iron pool and is essential for normal growth during iron limitation in Escherichia coli. Mol. Microbiol. *62*, 1181–1190.

Jiang, X., and Belasco, J.G. (2004). Catalytic activation of multimeric RNase E and RNase G by 5'-monophosphorylated RNA. Proc. Natl. Acad. Sci. USA *101*, 9211–9216.

Jost, D., Nowojewski, A., and Levine, E. (2013). Regulating the many to benefit the few: role of weak small RNA targets. Biophys. J. *104*, 1773–1782.

Kambara, T.K., Ramsey, K.M., and Dove, S.L. (2018). Pervasive targeting of nascent transcripts by hfq. Cell Rep. 23, 1543–1552.

Kass, R.E., and Wasserman, L. (1995). A reference bayesian test for nested hypotheses and its

relationship to the schwarz criterion. J. Am. Stat. Assoc. 90, 928-934.

Kohn, H., and Widger, W. (2005). The molecular basis for the mode of action of bicyclomycin. Curr. Drug Targets. Infect. Disord. *5*, 273–295.

Lavi-Itzkovitz, A., Peterman, N., Jost, D., and Levine, E. (2014). Quantitative effect of target translation on small RNA efficacy reveals a novel mode of interaction. Nucleic Acids Res. *42*, 12200–12211.

Levine, E., and Hwa, T. (2008). Small RNAs establish gene expression thresholds. Curr. Opin. Microbiol. *11*, 574–579.

Levine, E., Zhang, Z., Kuhlman, T., and Hwa, T. (2007). Quantitative characteristics of gene regulation by small RNA. PLoS Biol. *5*, e229.

Mackie, G.A. (1998). Ribonuclease E is a 5'-end-dependent endonuclease. Nature 395, 720–723.

Małecka, E.M., and Woodson, S.A. (2021). Stepwise sRNA targeting of structured bacterial mRNAs leads to abortive annealing. Mol. Cell.

Markham, N.R., and Zuker, M. (2005). DINAMelt web server for nucleic acid melting prediction. Nucleic Acids Res. 33, W577-81.

Massé, E., and Gottesman, S. (2002). A small RNA regulates the expression of genes involved in iron metabolism in Escherichia coli. Proc. Natl. Acad. Sci. USA 99, 4620–4625.

Massé, E., Escorcia, F.E., and Gottesman, S. (2003). Coupled degradation of a small regulatory RNA and its mRNA targets in Escherichia coli. Genes Dev. 17, 2374–2383.

Maurizi, M.R. (1992). Proteases and protein degradation in Escherichia coli. Experientia 48, 178–201.

Mehta, P., Goyal, S., and Wingreen, N.S. (2008). A quantitative comparison of sRNA-based and protein-based gene regulation. Mol. Syst. Biol. *4*, 221.

Mika, F., and Hengge, R. (2013). Small Regulatory RNAs in the Control of Motility and Biofilm Formation in E. coli and Salmonella. Int. J. Mol. Sci. *14*, 4560–4579.

Mitarai, N., Benjamin, J.-A.M., Krishna, S., Semsey, S., Csiszovszki, Z., Massé, E., and Sneppen, K. (2009). Dynamic features of gene expression control by small regulatory RNAs. Proc. Natl. Acad. Sci. USA *106*, 10655–10659.

Mohanty, B.K., and Kushner, S.R. (2016). Regulation of mRNA Decay in Bacteria. Annu. Rev. Microbiol. *70*, 25–44.

Morita, T., Kawamoto, H., Mizota, T., Inada, T., and Aiba, H. (2004). Enolase in the RNA degradosome plays a crucial role in the rapid decay of glucose transporter mRNA in the response to phosphosugar stress in Escherichia coli. Mol. Microbiol. *54*, 1063–1075.

Morita, T., Maki, K., and Aiba, H. (2005). RNase E-based ribonucleoprotein complexes: mechanical basis of mRNA destabilization mediated by bacterial noncoding RNAs. Genes Dev. 19, 2176–2186.

Nitzan, M., Rehani, R., and Margalit, H. (2017). Integration of bacterial small rnas in regulatory networks. Annu. Rev. Biophys. *46*, 131–148.

Novick, R.P., Iordanescu, S., Projan, S.J., Kornblum, J., and Edelman, I. (1989). pT181 plasmid replication is regulated by a countertranscript-driven transcriptional attenuator. Cell *59*, 395–404.

Papenfort, K., and Vogel, J. (2009). Multiple target regulation by small noncoding RNAs rewires gene expression at the post-transcriptional level. Res. Microbiol. *160*, 278–287.

- Papenfort, K., Sun, Y., Miyakoshi, M., Vanderpool, C.K., and Vogel, J. (2013). Small RNA-mediated activation of sugar phosphatase mRNA regulates glucose homeostasis. Cell *153*, 426–437.
- Park, S., Zhang, J., Reyer, M.A., Zareba, J., Troy, A.A., and Fei, J. (2018). Conducting Multiple Imaging Modes with One Fluorescence Microscope. J. Vis. Exp.
- Park, S., Prévost, K., Heideman, E.M., Carrier, M.-C., Azam, M.S., Reyer, M.A., Liu, W., Massé, E., and Fei, J. (2021). Dynamic interactions between the RNA chaperone Hfq, small regulatory RNAs, and mRNAs in live bacterial cells. Elife *10*.
- Pédelacq, J.-D., Cabantous, S., Tran, T., Terwilliger, T.C., and Waldo, G.S. (2006). Engineering and characterization of a superfolder green fluorescent protein. Nat. Biotechnol. *24*, 79–88.
- Persson, F., Lindén, M., Unoson, C., and Elf, J. (2013). Extracting intracellular diffusive states and transition rates from single-molecule tracking data. Nat. Methods *10*, 265–269.
- Petzold, L. (1983). Automatic selection of methods for solving stiff and nonstiff systems of ordinary differential equations. SIAM J. Sci. and Stat. Comput. *4*, 136–148.
- Prévost, K., Desnoyers, G., Jacques, J.-F., Lavoie, F., and Massé, E. (2011). Small RNA-induced mRNA degradation achieved through both translation block and activated cleavage. Genes Dev. *25*, 385–396.
- Reyer, M.A., McLean, E.L., Chennakesavalu, S., and Fei, J. (2018). An automated image analysis method for segmenting fluorescent bacteria in three dimensions. Biochemistry *57*, 209–215.
- Rice, J.B., and Vanderpool, C.K. (2011). The small RNA SgrS controls sugar-phosphate accumulation by regulating multiple PTS genes. Nucleic Acids Res. 39, 3806–3819.
- Rice, J.B., Balasubramanian, D., and Vanderpool, C.K. (2012). Small RNA binding-site multiplicity involved in translational regulation of a polycistronic mRNA. Proc. Natl. Acad. Sci. USA *109*, E2691-8.
- Richards, G.R., Patel, M.V., Lloyd, C.R., and Vanderpool, C.K. (2013). Depletion of glycolytic intermediates plays a key role in glucose-phosphate stress in Escherichia coli. J. Bacteriol. *195*, 4816–4825.
- Schmiedel, J.M., Axmann, I.M., and Legewie, S. (2012). Multi-target regulation by small RNAs synchronizes gene expression thresholds and may enhance ultrasensitive behavior. PLoS One 7, e42296.
- Sedlyarova, N., Shamovsky, I., Bharati, B.K., Epshtein, V., Chen, J., Gottesman, S., Schroeder, R., and Nudler, E. (2016). sRNA-Mediated Control of Transcription Termination in E. coli. Cell *167*, 111–121.e13.
- Sheng, H., Stauffer, W.T., Hussein, R., Lin, C., and Lim, H.N. (2017). Nucleoid and cytoplasmic localization of small RNAs in Escherichia coli. Nucleic Acids Res. *45*, 2919–2934.
- Tran, C.N., Giangrossi, M., Prosseda, G., Brandi, A., Di Martino, M.L., Colonna, B., and Falconi, M. (2011). A multifactor regulatory circuit involving H-NS, VirF and an antisense RNA modulates transcription of the virulence gene icsA of Shigella flexneri. Nucleic Acids Res. 39, 8122–8134. Urban, J.H., and Vogel, J. (2007). Translational control and target recognition by Escherichia coli small RNAs in vivo. Nucleic Acids Res. 35, 1018–1037.
- Vanderpool, C.K., and Gottesman, S. (2004). Involvement of a novel transcriptional activator and small RNA in post-transcriptional regulation of the glucose phosphoenolpyruvate phosphotransferase system. Mol. Microbiol. *54*, 1076–1089.

Vanderpool, C.K., and Gottesman, S. (2007). The novel transcription factor SgrR coordinates the response to glucose-phosphate stress. J. Bacteriol. *189*, 2238–2248.

Vecerek, B., Moll, I., Afonyushkin, T., Kaberdin, V., and Bläsi, U. (2003). Interaction of the RNA chaperone Hfq with mRNAs: direct and indirect roles of Hfq in iron metabolism of Escherichia coli. Mol. Microbiol. *50*, 897–909.

Virtanen, P., Gommers, R., Oliphant, T.E., Haberland, M., Reddy, T., Cournapeau, D., Burovski, E., Peterson, P., Weckesser, W., Bright, J., et al. (2020). SciPy 1.0: fundamental algorithms for scientific computing in Python. Nat. Methods *17*, 261–272.

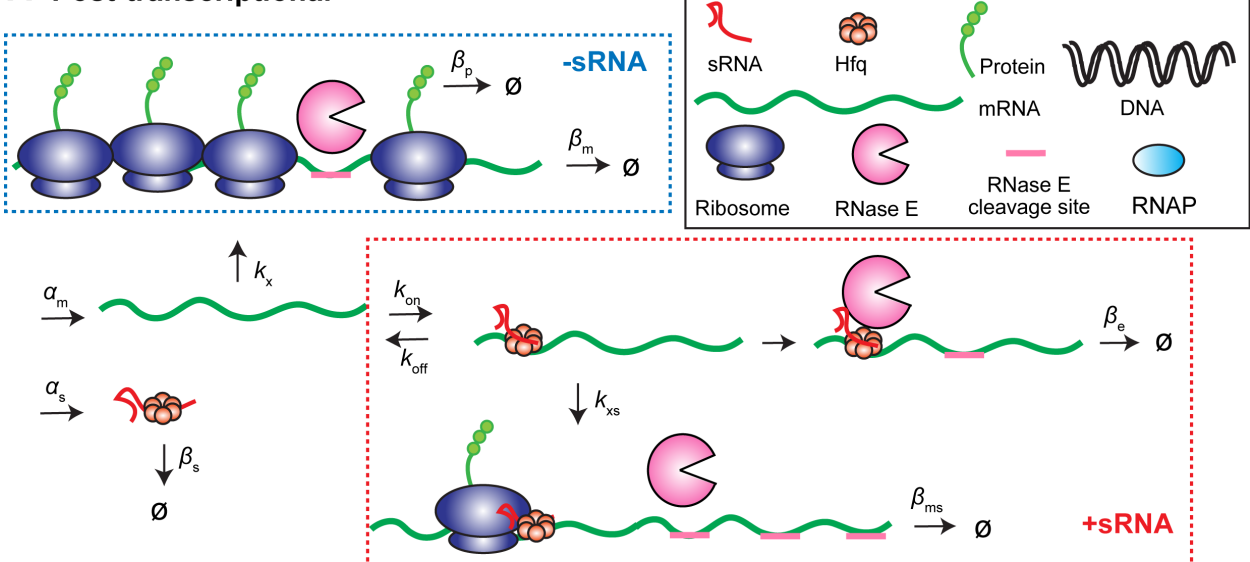
Wagner, E.G.H., and Romby, P. (2015). Small RNAs in bacteria and archaea: who they are, what they do, and how they do it. Adv Genet *90*, 133–208.

Yarchuk, O., Jacques, N., Guillerez, J., and Dreyfus, M. (1992). Interdependence of translation, transcription and mRNA degradation in the lacZ gene. J. Mol. Biol. 226, 581–596.

Young, R., and Bremer, H. (1976). Polypeptide-chain-elongation rate in Escherichia coli B/r as a function of growth rate. Biochem. J. *160*, 185–194.

Figure 1

A Post-transcriptional

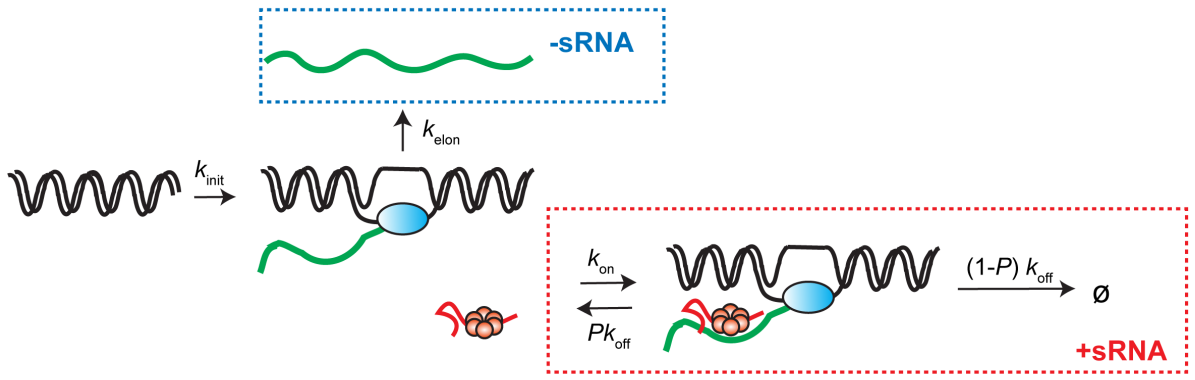


B Post-transcriptional

$$\frac{d[s]}{dt} = \alpha_{s} - \beta_{s}[s] - k_{on}[m][s] + k_{off}[ms] \qquad \frac{d[ms]}{dt} = k_{on}[m][s] - k_{off}[ms] - \beta_{ms}[ms] - \beta_{e}[ms]$$

$$\frac{d[m]}{dt} = \alpha_{m} - \beta_{m}[m] - k_{on}[m][s] + k_{off}[ms] \qquad \frac{d[p]}{dt} = k_{x}[m] + k_{xs}[ms] - \beta_{p}[p]$$

C Co-transcriptional



D Co-transcriptional

$$\begin{split} \frac{\mathrm{d}[\mathbf{s}]}{\mathrm{dt}} &= \alpha_{\mathrm{s}} - \beta_{\mathrm{s}}[\mathbf{s}] - k_{\mathrm{on}}([\mathbf{m}][\mathbf{s}] + [\mathbf{m}i][\mathbf{s}]) + k_{\mathrm{off}}([\mathbf{m}\mathbf{s}] + [\mathbf{m}i\mathbf{s}]) \\ \frac{\mathrm{d}[\mathbf{m}i]}{\mathrm{dt}} &= k_{\mathrm{elon}}[\mathbf{m}i] - \beta_{\mathrm{m}}[\mathbf{m}] - k_{\mathrm{on}}[\mathbf{m}][\mathbf{s}] + k_{\mathrm{off}}[\mathbf{m}\mathbf{s}] \\ \frac{\mathrm{d}[\mathbf{m}\mathbf{s}]}{\mathrm{dt}} &= k_{\mathrm{on}}[\mathbf{m}][\mathbf{s}] - k_{\mathrm{off}}[\mathbf{m}\mathbf{s}] -$$

